

Article

Antisymmetric Mode Cancellation for High-Q Cavities in a Double-Disk

Seung Hyeon Hong, Young Jin Lee, Seokhyeon Hong, Youngsoo Kim and Soon-Hong Kwon * 

Department of Physics, Chung-Ang University, 84, Heukseok-ro, Dongjak-gu, Seoul 06974, Korea

* Correspondence: shkwon@cau.ac.kr; Tel.: +82-2-820-5844

Abstract: High-quality factor dielectric microcavities like whispering-gallery-mode resonators can be widely applied in fields such as laser, optical sensor, switch, and filter. We propose the whispering-gallery-mode double-disk cavity comprising dielectric disks apart along the face of the disk. The electric field of each disk with opposite phases was excited; the emitted radiation field was annihilated by destructive interference. We numerically achieved a 5.67-fold enhancement in quality factor at the double-disk cavity with a radius, thickness, and gap distance of 850 nm, 220 nm, and 220 nm, respectively, compared to a single dielectric disk with the same structural conditions.

Keywords: whispering gallery modes; dielectric disk cavity; quality factor enhancement; destructive interference

1. Introduction

The study on a dielectric optical microcavity with a high quality (Q) factor has a long tradition of creating a structure where light and matter interact well. Various studies have been performed to retain the light in the cavity for a long time, such as photonic crystals [1–4], Fabry–Pérot cavities [5], and whispering gallery mode (WGM) resonators [6–24].

Primarily, WGM resonators use the confinement of light by total internal reflection at the interface of dielectric cavities, such as microdisk, ring, sphere, and toroid [6–24]. They are used as lasers [6–8], sensors [9,10], add/drop filters [11,12], single-photon sources [13], and optical switches [14,15] because they have a reasonably significant Q factor due to well-balanced radiation pattern and a simple structure. Recently, ultrahigh Q factors larger than 10^6 have been reported in the WGM resonators in the experiments and theoretical models [16–19]. Very recently, WGMs are exploited in highly developed sensing techniques such as single molecule level biological sensing [20], bio-electrostatic sensing [21], high sensitive gas sensing [22], temperature/pressure/biochemical sensing [23], and photonic labels into biological materials [24].

However, severe radiation loss limits the Q factor because the cavity size decreases to a wavelength size. Many studies have recently been proposed to increase the Q factor of the WGM resonator [25–30]. The methods to change the WGM resonator structure to suppress radiation loss, modifying the shape of the cavity from classical designs, such as adding distributed Bragg reflector (DBR) [25], mixing with a photonic crystal structure [26–28], and changing cavity form to micro gear shape [29,30], have been proposed. However, these methods do not only have cavities that outsize physical size but also have complicated designs.

However, the high Q factor of a simple-shaped dielectric rod has been reported without introducing additional structure by canceling radiation through the coupling of the improved Q factor [31–34]. However, it is required to carefully find the certain structure parameters that satisfy the coupling with BIC.

We propose a simple cavity consisting of two WGM dielectric disks to enhance the Q factor. The proposed structure does not require an additional structure to suppress radiation



Citation: Hong, S.H.; Lee, Y.J.; Hong, S.; Kim, Y.; Kwon, S.-H. Antisymmetric Mode Cancellation for High-Q Cavities in a Double-Disk. *Photonics* **2022**, *9*, 572. <https://doi.org/10.3390/photonics9080572>

Received: 19 July 2022

Accepted: 12 August 2022

Published: 14 August 2022

Publisher's Note: MDPI stays neutral with regard to jurisdictional claims in published maps and institutional affiliations.



Copyright: © 2022 by the authors. Licensee MDPI, Basel, Switzerland. This article is an open access article distributed under the terms and conditions of the Creative Commons Attribution (CC BY) license (<https://creativecommons.org/licenses/by/4.0/>).

or a delicate design to couple BIC. Simple form, arranging two identical dielectrics with a small vertical gap, can be a novel path to construct the high Q factor WGM cavities.

This study proposes a dielectric WGM double-disk cavity structured as two dielectric disks with the same radius (R), thickness (t), and gap distance (g) with the direction perpendicular to the face of the disk. Q was enhanced by approximately 5.67 times in this WGM cavity with $R = 850$ nm, $t = 220$ nm, and $g = 220$ nm compared to a single WGM disk with the equivalent radius and thickness. We investigated the improvement mechanism of the Q factor in terms of far-field radiation patterns and near-field profiles. Additionally, the dependence on different azimuthal numbers was also calculated.

2. Materials and Methods

The proposed cavity consisted of two disks with the same radius R , thickness t , and a gap distance g in the direction perpendicular to the plane of the disk. The refractive index of the dielectric disk was 3.48, which is the value of silicon at telecommunication wavelength; the disk was surrounded by air, as shown in Figure 1. We theoretically investigated the optical properties of the cavity, Q factors, mode profiles, and radiation patterns. All simulations were performed using commercial three-dimensional (3D) finite element method (FEM, COMSOL Multiphysics) software. We used the x-polarized plane-wave source to excite transverse-electric (TE)-like WGM; furthermore, the boundary condition was the scattering boundary condition (SBC).

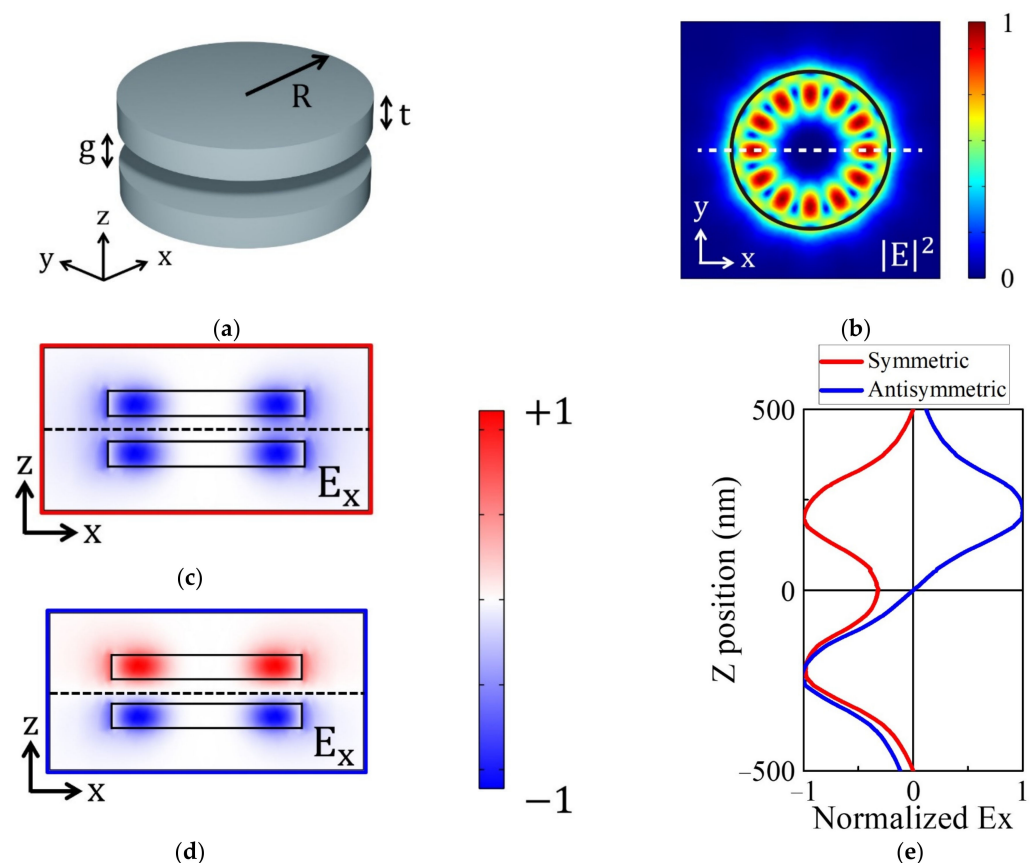


Figure 1. (a) Schematic diagram of the double-disk cavity. R , t , and g indicate the radius, thickness of the dielectric disk, and the size of the gap between two disks, respectively; (b) Horizontal views of the normalized electric field ($|E|^2$). The cross-sectional views of an electric field (E_x) profiles of the: (c) symmetric and (d) antisymmetric TE-like WGM modes with the azimuthal number, $m = 6$ for the cavity with $R = 850$ nm, $t = 220$ nm, and $g = 220$ nm. The black dashed lines indicate the center of cavity ($z = 0$ nm). The electric field is normalized as ± 1 as represented in the color bar. (e) The electric field (E_x) graph of the symmetric and antisymmetric modes along the z -axis.

The shape of the grid was tetrahedron; its size range was $\sim 0.006 \lambda/n - 0.2 \lambda/n$, where λ denotes resonance wavelength and n corresponds to the refractive index of materials.

We used 4-fold symmetry for analytical convenience and to fix the phase of WGM by setting a perfect magnetic conductor (PMC) at the XZ plane. The perfect electric conductor (PEC) or PMC was formed in the YZ plane depending on the odd or even azimuthal number, respectively. The electric field in the radial direction appearing in the TE-like WGM always appears at the maximum intensity in the XZ plane due to the PMC layer in the XZ plane.

Equation (1) was used to evaluate the change in the Q factor of the cavity with different gap distances.

$$Q = \frac{\nu}{2 \cdot \text{Im}(k_0)} \quad (1)$$

where Q denotes the Q factor of the cavity, ν corresponds to the resonance frequency, and k_0 is wave number in free space.

3. Results and Discussion

Figure 1a shows a schematic diagram of the dielectric double-disk cavity in which two dielectric disks with the same radius of R and thickness t were disposed of perpendicular to the disk's surface by the gap distance g.

Generally, two types of WGM are excited in a single dielectric disk: TE-like WGM and transverse-magnetic (TM)-like WGM. The TE-like WGM contains the perpendicular magnetic field to the disk surface and the electric field in the radial direction dominantly at the middle of the disk; TM-like WGM excites the electric field in the direction perpendicular to the face of the disk [35]. When the gap in the double-disk TM-like WGM is small, the electric field is intensely concentrated in the air slot region [12]. However, this study focused only on TE-like WGM because the symmetry of the electric fields of upper and lower disks in TM-like WGM weakly affected Q. Double disk TM-like WGM exhibited Q enhancement due to only a higher effective index with decreasing gap to less than 50 nm, and not due to the symmetry of the electric fields.

Since we design the cavity with a diameter similar to one target wavelength, operating at telecommunication wavelength, the radius of the single disk, R, was set to 850 nm so that the resonance is 1530 nm. The thickness, t, is assumed as 220 nm, half of the target wavelength in the material, which is the single slab waveguide mode condition. Within this condition, the TE-like WGM with azimuthal mode number $m = 6$ in a single disk cavity with $R = 850$ nm and $t = 220$ nm was excited at the wavelength of 1530 nm with a Q factor of 6600, as shown in Figure 1b. In general, there can be material absorption and radiation losses, however, in the proposed cavity, the absorption of the assumed material, silicon, is negligible at the target wavelength so that only radiation loss is considered. The Q factor was calculated by Equation (1) based on the estimation of the imaginary wave number in the mode solver of the FEM simulation. As R increases, the resonance red-shifts linearly and the Q factor is mostly maintained for the mode with the same azimuthal number. On the other hand, as t increases, the resonance, red-shift, and the Q factor increases due to a higher effective index.

We placed an identical dielectric disk on the single disk cavity with an air gap to use the symmetry of the mode to enhance the Q factor. In the double-disk cavity with $R = 850$ nm, $t = 220$ nm, and $g = 220$ nm, two combined TE-like WGMs were excited near the wavelength of 1500 nm for the same azimuthal number with different symmetries. Figure 1c,d show the E_x electric field profiles corresponding to the radial direction of the disk in the XZ plane of the double-disk cavity, indicated by the white dashed line in Figure 1b.

Figure 1c shows a symmetric mode in which the electric field phase of two disks is the same. Furthermore, Figure 1d shows an antisymmetric mode with a phase difference of 180° between each dielectric disk. In the middle of the two disks, the electric field intensity node indicated by the narrow white region between the upper red and lower

blue colored fields was found due to destructive interference of upper and lower TE-like WGMs. Figure 1e shows the E_x electric field of two modes along the z -axis in the range from -500 nm to 500 nm at the electric field maximum in the x -axis ($x = 650$ nm) in Figure 1c,d. Here, the antisymmetric mode shows that the electric field intensity is zero at $z = 0$ due to destructive interference, different from the symmetric mode.

We investigated the optical properties of the symmetric and antisymmetric modes as a function of gap distance, g . The Q factor and the resonant wavelength changed based on the change in g because of changing the amount of interaction of the electric field in the radial direction inside the disk for each symmetric and antisymmetric mode (see Figure 2).

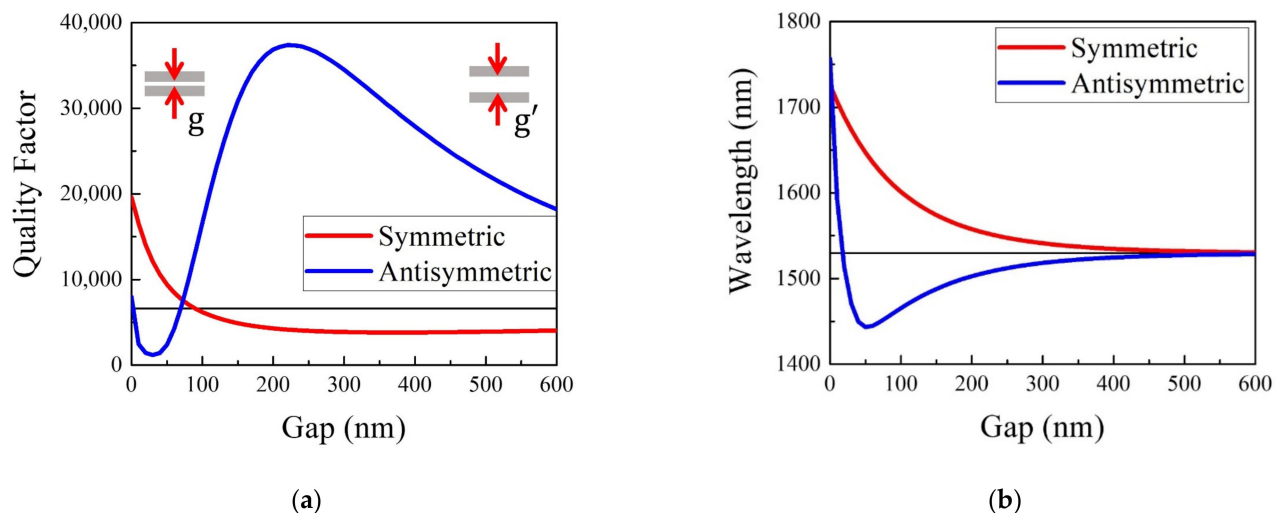


Figure 2. (a) Q factors and (b) the resonant wavelength of the symmetric (red) and antisymmetric (blue) modes based on $m = 6$ TE-like WGM for different gap sizes. The black line indicates the values of single disk TE-like WGM.

Figure 2 shows the Q factor and resonance wavelength of symmetric and antisymmetric modes when g was increased from 0 nm to 600 nm with an interval of 10 nm. The red curves indicate the symmetric mode of the Q factor and resonance wavelength. At $g = 0$ nm, where two disks were attached, the highest Q factor of 20,000 and the longest wavelength of 1730 nm were obtained. The resonant wavelength decreased with an increasing gap and approaches to the value of the single disk mode. In the case of the symmetric mode, a small gap structure can be understood as a thicker single disk WGM, resulting in a higher Q factor and longer resonant wavelength. The coupling of two TE-like WGMs of the upper and lower disks causes the mode to split into symmetric and antisymmetric modes in the spectrum and the shorter and longer resonant wavelengths than that of the single disk are represented, as shown in Figure 2b.

Furthermore, the Q factor of the antisymmetric mode showed a dramatic change in the value. At $g = 220$ nm, the Q factor had a maximum value of 37,000, which is 5.6 times larger than the Q factor (6600) of the single TE-like WGM. In most of the gap regions larger than 30 nm, the single maximum peak was observed at $g = 220$ nm. The Q factor decreased and would approach the Q factor of the single disk, with an increasing gap. The resonance wavelength increased rapidly in the narrow region of $g = 0$ –30 nm. Moreover, the Q factor also increased with increasing g to 0 nm. In both symmetric and antisymmetric modes, the resonant wavelengths approached the wavelength of the single disk with an increasing gap.

We investigated the electric field intensity profiles and vector plots in the cross-sectional view of the XZ plane and the radiation patterns in Figure 3 to understand the different gap dependences of the Q factor and the resonant wavelength of the symmetric/antisymmetric modes. Figure 3a,c show symmetric mode profiles with a gap distance of 30 nm and 220 nm. The vector plots of the electric fields excited in the two dielectric disks

exhibited the same phase (see Figure 3a,c). Therefore, the symmetric mode of $g = 30$ nm and 220 nm shows similar radiation patterns as single TE-like WGM in the normalized far-field patterns of Figure 3e, having the strongest radiation at 90° and 270° , to the direction of the plane of the disk.

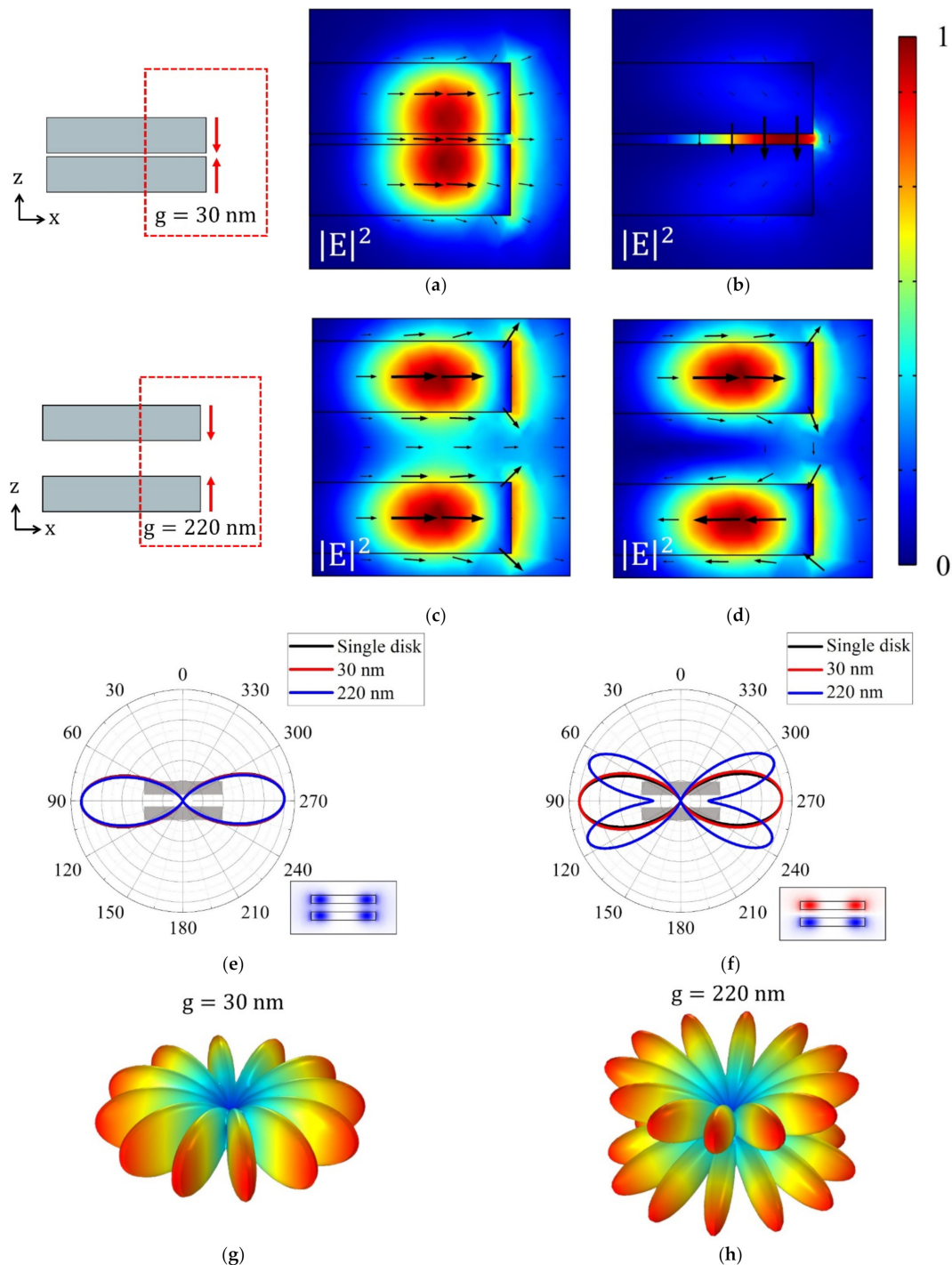


Figure 3. The electric field intensity mode profiles of the (a) symmetric and (b) antisymmetric modes with g of 30 nm and (c) symmetric and (d) antisymmetric modes with g of 220 nm. The black arrows in the figures show the electric field vector. The normalized far-field patterns in the cross-section in XZ plane show the radiation properties of the (e) symmetric, (f) antisymmetric modes for $g = 30$ nm (red) and $g = 220$ nm (blue). The black line indicates the far-field pattern of the single disk. 3D far-field patterns of antisymmetric mode for (g) $g = 30$ nm and (h) $g = 220$ nm.

However, most electric fields were strongly confined inside the disk for $g = 30$ nm (Figure 3a), and a non-negligible electric field was observed outside of the upper and lower surfaces of two disks for the $g = 220$ nm (Figure 3c). A higher Q factor and longer resonant wavelength of the symmetric mode at a smaller gap were originated from the stronger confinement of the mode inside dielectric disks, having a higher effective index and, consequently, less radiation loss.

We assumed that the dielectric disk had the same spatial condition and azimuthal number. In the case of symmetric WGM, the highest Q factor can be achieved due to the suppressed radiation loss when the effective refractive index, n_{eff} —the refractive index that light experiences relative to the structure—is the largest. At $g = 0$ nm, dielectric disks were attached, and the thickness of the disk was doubled; the maximum Q factor of the symmetric mode was obtained because of a higher effective index. Equation (2) is used to calculate the resonance wavelength of WGM [8].

$$2\pi n_{eff}R = m\lambda \quad (2)$$

We found using Equation (2) that it had the longest resonance wavelength with a maximum n_{eff} at $g = 0$ nm. The grown gap area decreased effective index with increasing gap distance, causing a reduction in Q factor and resonance wavelength. Briefly, the Q factor of the symmetric mode was found to be mainly affected by the effective index. According to Equation (2), the effective refractive indices of the symmetric and antisymmetric modes are 1.88 and 1.65 at the $g = 30$ nm and they become 1.74 and 1.69 at $g = 220$ nm, respectively.

According to Equation (2), as the radius (R) increases, the resonance wavelength increases linearly. For example, the resonances are 1372 nm, 1500 nm, and 1632 nm for $R = 750, 850$, and 950 nm, respectively, while t and g are fixed to 220 nm and 220 nm. Similarly, the resonance depends on the thickness of the disk linearly. The resonances are 1472 nm, 1500 nm, and 1537 nm for $t = 200, 220$, and 240 nm, respectively, for the cavity with $R = 850$ nm and $g = 220$ nm.

Radiation patterns of the symmetric mode in the far-field patterns of the symmetric mode (Figure 3e) were approximately identical in different gap sizes and also similar to that of the single disk. The divergence angle of the radiation decreased slightly with an increasing gap due to the effectively larger thickness of the disk; however, the difference was negligible.

Figure 3b,d show characteristics of the electric field in the antisymmetric mode of the double disk cavity, which shows normalized electric field and vector in the XZ plane. Figure 3d shows the antisymmetric mode at $g = 220$ nm. The opposite electric fields of upper and lower disks interfere destructively such that the radiation loss along the horizontal direction—the main emission direction of WGM in the disk—is strongly suppressed and the Q factor can be enhanced. The maximum Q factor appeared at $g = 220$ nm when the degree of destructive interference was most significant.

Figure 3f–h show the normalized far-field pattern for g of 30 nm and 220 nm in the antisymmetric mode. The far-field pattern at $g = 30$ nm was similar to that of the single TE-like WGM. However, the far-field graph of $g = 220$ nm showed the intensity dips at 90° and 270° , unlike horizontal radiation of the symmetric mode and the single disk WGM in which the emission directions were 90° and 270° . The radiation to the horizontal direction, the main emission direction of the disk WGM, dropped significantly due to the suppression of field radiation by destructive interference of the opposite electric fields of the upper and lower disks. Q enhancement of the cavity can be observed because the main radiation loss was suppressed. When the gap distance was longer than 220 nm, the incident light recognized dielectric disks of the cavity as separate structures regardless of the modes. Therefore, the Q factor and resonance wavelength of both modes were saturated to the black line of the graph corresponding to the single TE-like WGM mode's values.

When two disks were attached, the Q factor and resonance wavelength increased sharply in the region of $g = 0$ –30 nm due to the thick cavity. The antisymmetric mode showed strong E_z field in the middle of the gap when the gap was very narrow, such as

$g = 30$ nm, as shown in Figure 3b. The strong electric field was excited in the diagonal direction at the edge of the disk due to the edge effect [36]. Electric fields emitted from each disk edge contained an identical E_z field and a contradictory E_x field. Hence, the strong E_z field remained in the gap of the cavity due to electric field vector summation. Moreover, the E_z field was sufficiently enhanced to ignore the destructive interference effect. Therefore, the destructive interference was not critical property in the $g = 0$ –30 nm where there is no gap or narrow. Therefore, the Q factor and resonance wavelength drastically decreased in a similar form as the symmetric mode with expanding gap area.

The Q factor of TE-like WGM on $m = 6$ single dielectric disk was 6600; the highest Q factors of the symmetric and antisymmetric mode were 19,600 ($g = 0$ nm) and 37,400 ($g = 220$ nm), respectively. Therefore, the Q factor can be enhanced in the symmetric and antisymmetric modes by approximately 2.97 times by 5.67 times larger than that of the single disk TE-like WGM.

We analyzed enhancement in the Q factor compared to a single disk when the azimuthal number was changed with a focus on increasing the Q factor by destructive interference with the same structural condition.

We analyzed the amount of enhancement in the Q factor compared to that of the single disk for different azimuthal numbers with a focus on increasing the Q factor by destructive interference with the same structural condition, as shown in Figure 4a.

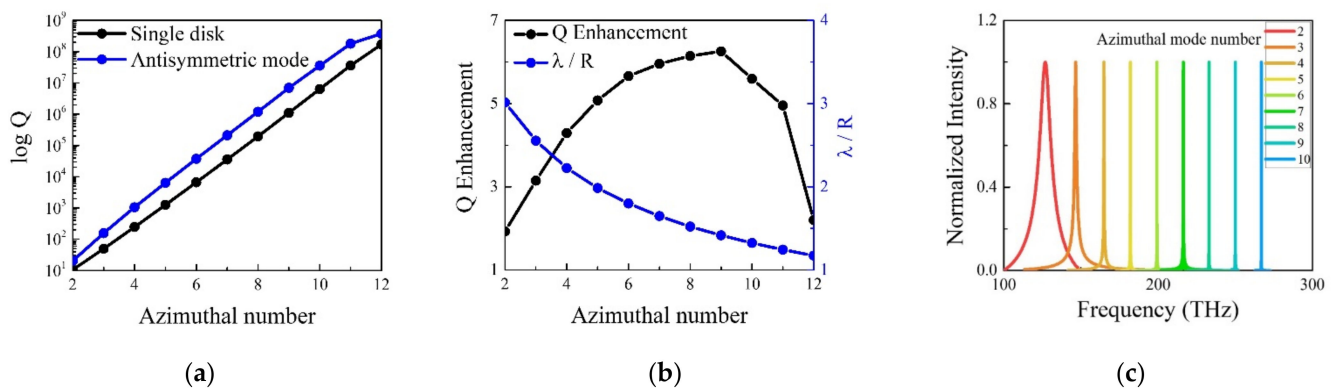


Figure 4. (a) The log-scaled quality factors of the single disk (black) and an antisymmetric TE-like WGM (blue); (b) The Q factor enhancement and the normalized resonance wavelength of the antisymmetric TE-like WGM. Q factor was normalized by the Q of the single disk TE-like WGM. The wavelength was normalized by the disk radius. (c) The spectrum of the antisymmetric mode for different azimuthal number, m . The structure was fixed to $R = 850$ nm, $t = 220$ nm, and $g = 220$ nm.

While the disk radius, thickness, and gap distance were fixed to 850 nm, 220 nm, and 220 nm, respectively, the azimuthal number of an antisymmetric mode varied from 2 to 12 as the resonance wavelength decreased from 2400 nm to 1000 nm. Figure 4a shows the Q factor in log-scale for the single TE-like WGM and the double disk antisymmetric mode with an increasing azimuthal number. In both cases, the Q factors increased exponentially with the azimuthal number. For example, when the m increased from 2 to 12, the single disk showed the Q factor increment from 11 to 1.7×10^8 and the double disk antisymmetric cavity showed that from 21 to 3.8×10^8 .

For a detailed Q factor enhancement of the double disk antisymmetric mode to the single disk TE-like mode, we calculated the Q enhancement (see Figure 4b), the Q factor of the antisymmetric mode by dividing the single disk's value.

The Q factor did improve by 1.9 times at $m = 2$ than a single disk. Hence, the incident light with a wavelength of 2400 nm, which is longer than double-disk radii, recognized the cavity as a single structure. Therefore, the degree of Q factor enhancement was lower compared to higher m .

The incident light identified the cavity as composed of two disks with increasing m because of decreasing resonance wavelength. Therefore, a maximum enhancement

in Q of approximately 6.3 was achieved at $m = 9$. When the m was larger than 10, the resonance wavelength became shorter. The fixed gap of 220 nm was effectively larger than the resonance wavelength. Hence, the influence of destructive interference—the main reason for the Q factor enhancement in the TE-like antisymmetric WGM mode—was reduced, as shown in the region of g larger than 220 nm in Figure 2a. Consequently, the Q factor decreased.

Figure 4c shows the spectrum of the antisymmetric mode for different azimuthal numbers of the proposed cavity with the fixed $R = 850$ nm, $t = 220$ nm, and $g = 220$ nm. As the value of m increases from 2 to 10, the peak exhibits narrower linewidth due to a higher Q factor and the resonance frequency increases with a regular frequency spacing (free spectral range). The characteristic free spectral range of WGM is clearly visible.

In order to take into account the fabrication suitability of the proposed cavity, we investigated Q factors as functions of the fabrication errors, radius, and thickness of one disk, in the tolerance range of ± 20 nm for the antisymmetric mode in a double disk cavity with $R = 850$ nm, $t = 220$ nm, and $g = 220$ nm. We assumed the lower disk has a larger radius or thickness than the R and t of the upper disk with the amounts of ΔR or Δt , as indicated in Figure 5a,b. Δg means the change of the gap distance from $g = 220$ nm, which is already investigated in Figure 2. When ΔR and Δt are -20 nm, the Q factors drop to 24,500 and 15,200. The fabrication errors of R and t cause a decrease in the Q factor because the balance of the radiation field between two disks is broken, as shown in Figure 5c. On the other hand, Δg does not significantly affect the Q factor in the range of 20 nm. Considering the fabrication process of the wafer growth and the thin film deposition, the gap distance and the thickness of the disks can be fabricated with high accuracy. Since e-beam lithography and dry etching will determine the radius and the accuracy can be worst in the R , t , and g , the controls of the radius of the upper and lower disks would be important in the performance of the proposed cavity.

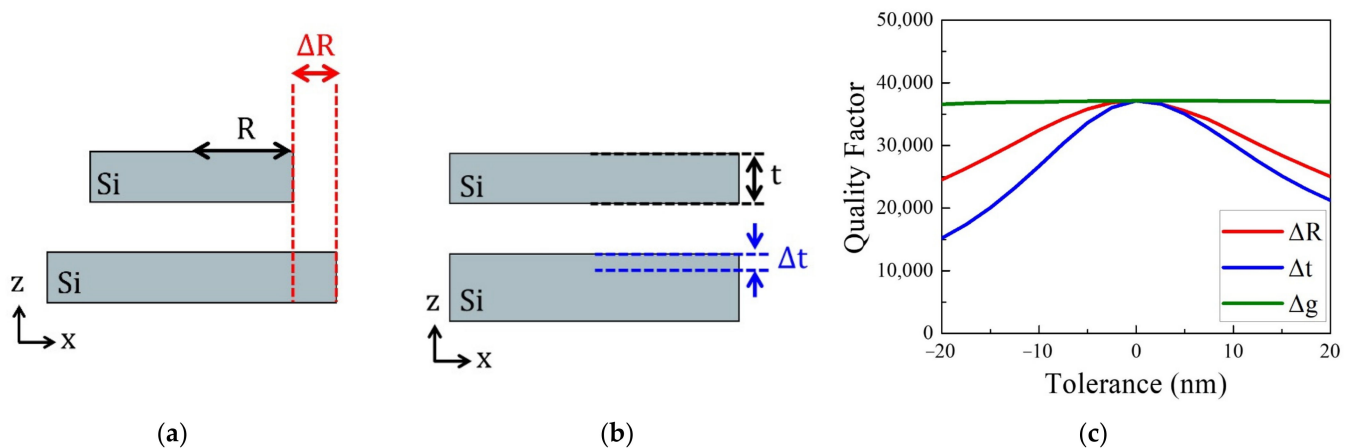


Figure 5. (a) Schematic diagrams of a double disk cavity with fabrication errors of (a) radius and (b) thickness. In both cases, the lower disk has a larger radius or thickness. (c) Q factors are investigated as functions of the fabrication tolerances for the antisymmetric mode in the cavity with $R = 850$ nm, $t = 220$ nm, and $g = 220$ nm. The ΔR , Δt , and Δg indicate the fabrication errors of radius, the thickness of the lower disk, and the gap distance of the double disk cavity, respectively.

If both disks have the same larger refractive index, the Q factor will be enlarged due to the suppression of radiation loss and the resonance will red-shift as generally observed in the common WGMs. However, if the refractive indices of two disks are different, the electric field intensities of the upper and lower modes are different and the destructive interference of the antisymmetric modes becomes weaker, resulting in the reduction of the cavity Q -factor, likewise in the case of a different radius of two disks of Figure 5.

We could consider a double disk cavity with a low index central pillar placed between upper and lower disks to obtain the double disk with an air gap. If the diameter of the pillar

is sufficiently small such that it does not influence the WGM, the antisymmetric TE-like WGM can be supported regardless of the existence of the central pillar because the electric field of the TE-like WGM is mostly placed at the edge of the disk. When buffered oxide wet etching is applied to a double silicon-rich nitride cavity with a thin SiO₂ gap layer, only the edge of the SiO₂ layer is removed [37].

In order to have the possibility of manufacturing the proposed cavity with a disk radius less than 1 μm and a low index pillar, we investigated the Q factor dependence on the radius of the pillar in Figure 6. As shown in Figure 6a, the low index pillar has a radius of R_p slightly smaller than the disk radius, R , and the refractive index of the pillar was set to 1.48, which is the value of SiO₂ at telecommunication wavelength. For the antisymmetric mode with $m = 6$ in the cavity of $R = 850$ nm, $t = 220$ nm, and $g = 220$ nm, the Q factor, and the resonant wavelength are investigated when the pillar radius varies from 0 to 900 nm (Figure 6b). The Q factor and resonance wavelength are almost maintained in the region from 0 to 700 nm. $R_p = 0$ nm indicates just an air gap between two disks. At $R_p > 700$ nm, Q factor decreased dramatically. Considering the realization of the proposed cavity, if the radius of the low index pillar is smaller than 700 nm, the performance of the cavity such as the Q factor is maintained. Therefore, careful selective wet etching can control the pillar size in the fabrication of the cavity, as reported in the sub-micrometer pillar of the photonic crystal laser [38] and the microdisk [39]. The tolerance of the pillar size of 700 nm would make the realization of the proposed cavity feasible. If the cavity is placed above the additional pillar on the substrate and the height is large enough to minimize the leakage radiational loss to the substrate, the radius of the pillar also affects the Q factor similarly.

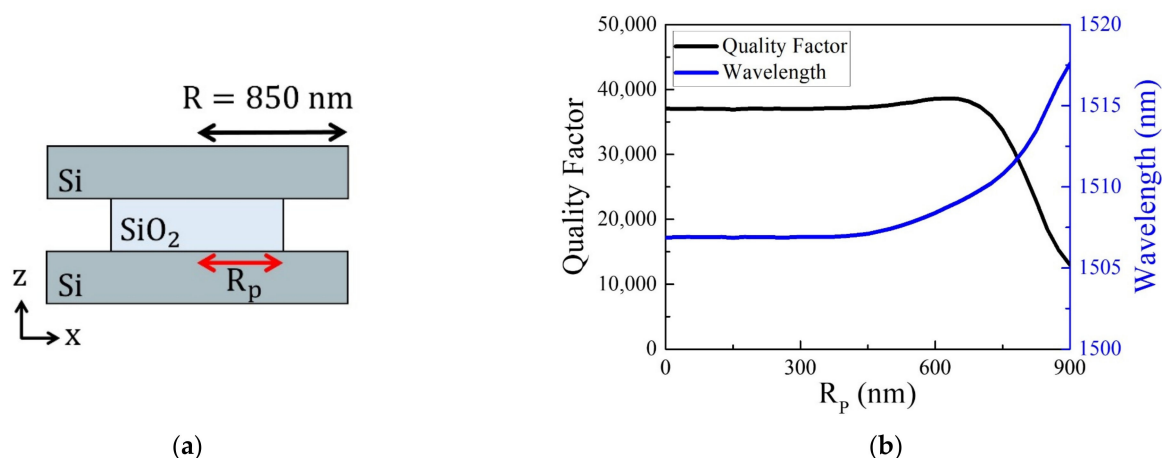


Figure 6. (a) Schematic diagram of the double-disk cavity with a low index central pillar placed in the gap. R_p indicates the radius of the pillar. (b) The Q factor and the resonance wavelength of the antisymmetric mode as functions of the pillar radius with the fixed condition of $R = 850$ nm, $t = 220$ nm, and $g = 220$ nm.

Likewise single microdisk or ring cavities, the passive double-disk cavity also can be excited by optical fiber [40–42] or nano-waveguide [43,44] coupled with an external light source. On the other hand, if the proposed cavity is operated as the active light source such as a nano-laser, the cavity can be excited by various gain materials, quantum dots [41,45,46], quantum wells [47], and nanowires [48].

4. Conclusions

In summary, this study proposes a double disk cavity with a radius of 850 nm and a disk thickness of 220 nm. We investigated the Q factor enhancement of the antisymmetric mode compared with the single disks. We observed a 5.67-fold enhancement in the Q factor for the resonant wavelength of 1510 nm of the TE-like WGM with an azimuthal number of 6. The suppression of main radiation loss was analyzed through the far-field radiation patterns.

Quasi-BIC structures and our double-disk cavity use a similar approach to improve the Q factor: the suppression of the radiation loss due to destructive interference. The case of Quasi-BIC structures declines the radiation field by destructive interference between different types of modes that are excited within the cavity [31,49]. It is challenging to analyze emerging conditions because two or more different modes in the structure must be excited and offset and the cavity satisfying the requirement is limited.

However, our cavity reduced the radiation field emitted from the entire structure by exciting the antisymmetric WGM of each dielectric disk with identical conditions—the wavelength in the same disks. Due to the condition that only two WGM should be formed with out-of-phase, it can be operated even in a simple design and is easy to interpret.

The destructive interference of the field occurring in distant structures can be used easily in practical applications. It means that not only dielectric disks simulated in this study but also toroids, rings, truncated cones, and complex forms, such as photonic crystal rings, which can excite WGM, can achieve strong Q enhancement by placing two same geometrical cavities.

Author Contributions: Investigation, S.H.H.; Methodology, S.H. and S.-H.K.; Supervision, S.-H.K.; Validation, Y.J.L., S.H., Y.K. and S.-H.K.; Writing—original draft, S.H.H. All authors have read and agreed to the published version of the manuscript.

Funding: This research was supported by the Chung-Ang University Research Scholarship Grants in 2021 and the National Research Foundation of Korea through the Korean Government under Grants NRF-2021R1F1A1047119.

Institutional Review Board Statement: Not applicable.

Informed Consent Statement: Not applicable.

Data Availability Statement: Not applicable.

Conflicts of Interest: The authors declare no conflict of interest.

References

1. Akahane, Y.; Asano, T.; Song, B.S.; Noda, S. High-Q Photonic Nanocavity in a Two-Dimensional Photonic Crystal. *Nature* **2003**, *425*, 944–947. [\[CrossRef\]](#) [\[PubMed\]](#)
2. Quan, Q.; Loncar, M. Deterministic Design of Wavelength Scale, Ultra-High Q Photonic Crystal Nanobeam Cavities. *Opt. Express* **2011**, *19*, 18529–18542. [\[CrossRef\]](#) [\[PubMed\]](#)
3. Liang, H.; Jiang, H.; Lin, Q.; Luo, R.; He, Y. High-Quality Lithium Niobate Photonic Crystal Nanocavities. *Optica* **2017**, *4*, 1251–1258. [\[CrossRef\]](#)
4. Srinivasan, K.; Painter, O. Momentum Space Design of High-Q Photonic Crystal Optical Cavities. *Opt. Express* **2002**, *10*, 670–684. [\[CrossRef\]](#) [\[PubMed\]](#)
5. Hunger, D.; Steinmetz, T.; Colombe, Y.; Deutsch, C.; Hänsch, T.W.; Reichel, J. A Fiber Fabry-Perot Cavity with High Finesse. *New J. Phys.* **2010**, *12*, 065038. [\[CrossRef\]](#)
6. Shitikov, A.E.; Benderov, O.V.; Kondratiev, N.M.; Lobanov, V.E.; Rodin, A.V.; Bilenko, I.A. Microresonator and Laser Parameter Definition via Self-Injection Locking. *Phys. Rev. Appl.* **2020**, *14*, 064047. [\[CrossRef\]](#)
7. Grossmann, T.; Schleede, S.; Hauser, M.; Christiansen, M.B.; Vannahme, C.; Eschenbaum, C.; Klinkhammer, S.; Beck, T.; Fuchs, J.; Nienhaus, G.U.; et al. Low-Threshold Conical Microcavity Dye Lasers. *Appl. Phys. Lett.* **2010**, *97*, 063304. [\[CrossRef\]](#)
8. He, L.; Özdemir, Ş.K.; Yang, L. Whispering Gallery Microcavity Lasers. *Laser Photon. Rev.* **2013**, *7*, 60–82. [\[CrossRef\]](#)
9. Bianchetti, A.; Federico, A.; Vincent, S.; Subramanian, S.; Vollmer, F. Refractometry-Based Air Pressure Sensing Using Glass Microspheres as High-Q Whispering-Gallery Mode Microresonators. *Opt. Commun.* **2017**, *394*, 152–156. [\[CrossRef\]](#)
10. Zhu, J.; Ozdemir, S.K.; Xiao, Y.F.; Li, L.; He, L.; Chen, D.R.; Yang, L. On-Chip Single Nanoparticle Detection and Sizing by Mode Splitting in an Ultrahigh-Q Microresonator. *Nat. Photonics* **2010**, *4*, 46–49. [\[CrossRef\]](#)
11. Little, B.E.; Chu, S.T.; Haus, H.A.; Foresi, J.; Laine, J.P. Microring Resonator Channel Dropping Filters. *J. Light. Technol.* **1997**, *15*, 998–1005. [\[CrossRef\]](#)
12. Lee, Y.J.; Lee, D.E.; Kwon, S.H. Broadband Tunable Add/Drop Filters Based on Dielectric Double-Disk Microcavities. *IEEE Photonics J.* **2017**, *9*, 6601607. [\[CrossRef\]](#)
13. Dusanowski, Ł.; Köck, D.; Shin, E.; Kwon, S.H.; Schneider, C.; Höfling, S. Purcell-Enhanced and Indistinguishable Single-Photon Generation from Quantum Dots Coupled to On-Chip Integrated Ring Resonators. *Nano Lett.* **2020**, *20*, 6357–6363. [\[CrossRef\]](#)
14. Wen, Y.H.; Kuzucu, O.; Hou, T.; Lipson, M.; Gaeta, A.L. All-Optical Switching of a Single Resonance in Silicon Ring Resonators. *Opt. Lett.* **2011**, *36*, 1413–1415. [\[CrossRef\]](#)

15. Liu, L.; Kumar, R.; Huybrechts, K.; Spuesens, T.; Roelkens, G.; Geluk, E.J.; De Vries, T.; Regreny, P.; Van Thourhout, D.; Baets, R.; et al. An Ultra-Small, Low-Power, All-Optical Flip-Flop Memory on a Silicon Chip. *Nat. Photonics* **2010**, *4*, 182–187. [[CrossRef](#)]
16. Spencer, D.T.; Bauters, J.F.; Bowers, J.E.; Heck, M.J.R. Integrated Waveguide Coupled Si₃N₄ Resonators in the Ultrahigh-Q Regime. *Optica* **2014**, *1*, 153–157. [[CrossRef](#)]
17. Liu, K.; Jin, N.; Cheng, H.; Chauhan, N.; Puckett, M.W.; Nelson, K.D.; Behunin, R.O.; Behunin, R.O.; Rakich, P.T.; Blumenthal, D.J. Ultralow 0.034 DB/m Loss Wafer-Scale Integrated Photonics Realizing 720 Million Q and 380 MW Threshold Brillouin Lasing. *Opt. Lett.* **2022**, *47*, 1855–1858. [[CrossRef](#)]
18. Ciminelli, C.; Innone, F.; Brunetti, G.; Conteduca, D.; Dell’Olio, F.; Tatoli, T.; Armenise, M.N. Rigorous Model for the Design of Ultra-High Q-Factor Resonant Cavities. In Proceedings of the 2016 18th International Conference on Transparent Optical Networks (ICTON), Trento, Italy, 10–14 July 2016; pp. 1–4. [[CrossRef](#)]
19. Yang, K.Y.; Oh, D.Y.; Lee, S.H.; Yang, Q.F.; Yi, X.; Shen, B.; Wang, H.; Vahala, K. Bridging Ultrahigh-Q Devices and Photonic Circuits. *Nat. Photonics* **2018**, *12*, 297–302. [[CrossRef](#)]
20. Yu, D.; Humar, M.; Meserve, K.; Bailey, R.C.; Chormaic, S.N.; Vollmer, F. Whispering-Gallery-Mode Sensors for Biological and Physical Sensing. *Nat. Rev. Methods Prim.* **2021**, *1*, 82. [[CrossRef](#)]
21. Wang, Z.; Zhang, Y.; Gong, X.; Yuan, Z.; Feng, S.; Xu, T.; Liu, T.; Chen, Y.C. Bio-Electrostatic Sensitive Droplet Lasers for Molecular Detection. *Nanoscale Adv.* **2020**, *2*, 2713–2719. [[CrossRef](#)]
22. Lemieux-Leduc, C.; Guertin, R.; Bianki, M.-A.; Peter, Y.-A. All-Polymer Whispering Gallery Mode Resonators for Gas Sensing. *Opt. Express* **2021**, *29*, 8685–8697. [[CrossRef](#)] [[PubMed](#)]
23. Zhao, X.; Guo, Z.; Zhou, Y.; Guo, J.; Liu, Z.; Li, Y.; Luo, M.; Wu, X. Optical Whispering-Gallery-Mode Microbubble Sensors. *Micromachines* **2022**, *13*, 592. [[CrossRef](#)] [[PubMed](#)]
24. Capocéfalo, A.; Quintiero, E.; Conti, C.; Ghofraniha, N.; Viola, I. Droplet Lasers for Smart Photonic Labels. *ACS Appl. Mater. Interfaces* **2021**, *13*, 51485–51494. [[CrossRef](#)] [[PubMed](#)]
25. Nowicki-Bringuier, Y.-R.; Claudon, J.; Böckler, C.; Reitzenstein, S.; Kamp, M.; Morand, A.; Forchel, A.; Gérard, J.M. High Q Whispering Gallery Modes in GaAs/AlAs Pillar Microcavities. *Opt. Express* **2007**, *15*, 17291–17304. [[CrossRef](#)]
26. Hamidi, S.R.; Daraei, A. A Nanomaterial Sensor Based on Tapered Photonic Crystal Nanometer-Scale Cavity in a Microdisk. *Opt. Quantum Electron.* **2020**, *52*, 167. [[CrossRef](#)]
27. Ryu, H.Y.; Notomi, M.; Kim, G.H.; Lee, Y.H. High Quality-Factor Whispering-Gallery Mode in the Photonic Crystal Hexagonal Disk Cavity. *Opt. Express* **2004**, *12*, 1708–1719. [[CrossRef](#)]
28. Gao, G.; Zhang, Y.; Zhang, H.; Wang, Y.; Huang, Q.; Xia, J. Air-Mode Photonic Crystal Ring Resonator on Silicon-on-Insulator. *Sci. Rep.* **2016**, *6*, 19999. [[CrossRef](#)]
29. Fujita, M.; Baba, T. Microgear Laser. *Appl. Phys. Lett.* **2002**, *80*, 2051–2053. [[CrossRef](#)]
30. Lu, X.; McClung, A.; Srinivasan, K. High-Q Slow Light and Its Localization in a Photonic Crystal Microring. *Nat. Photonics* **2021**, *16*, 66–71. [[CrossRef](#)]
31. Bogdanov, A.A.; Koshelev, K.L.; Kapitanova, P.V.; Rybin, M.V.; Gladyshev, S.A.; Sadrieva, Z.F.; Samusev, K.B.; Kivshar, Y.S.; Limonov, M.F. Bound States in the Continuum and Fano Resonances in the Strong Mode Coupling Regime. *Adv. Photonics* **2019**, *1*, 016001. [[CrossRef](#)]
32. Bulgakov, E.N.; Pichugin, K.N.; Sadreev, A.F. Interaction between Dielectric Particles Enhances the Q Factor. *J. Phys. Conf. Ser.* **2020**, *1461*, 012144. [[CrossRef](#)]
33. Pichugin, K.; Sadreev, A.; Bulgakov, E. Ultrahigh-Q System of a Few Coaxial Disks. *Nanophotonics* **2021**, *10*, 4341–4346. [[CrossRef](#)]
34. Yang, H.; Chen, Y.; Liu, M.; Xiao, G.; Luo, Y.; Liu, H.; Li, J.; Yuan, L. High Q-Factor Hybrid Metamaterial Waveguide Multi-Fano Resonance Sensor in the Visible Wavelength Range. *Nanomaterials* **2021**, *11*, 1583. [[CrossRef](#)]
35. Ghulinyan, M.; Navarro-Urrios, D.; Pitanti, A.; Lui, A.; Pucker, G.; Pavesi, L. Whispering-Gallery Modes and Light Emission from a Si-Nanocrystal-Based Single Microdisk Resonator. *Opt. Express* **2008**, *16*, 13218–13224. [[CrossRef](#)]
36. Kneissl, M.; Teepe, M.; Miyashita, N.; Johnson, N.M.; Chern, G.D.; Chang, R.K. Current-Injection Spiral-Shaped Microcavity Disk Laser Diodes with Unidirectional Emission. *Appl. Phys. Lett.* **2004**, *84*, 2485–2487. [[CrossRef](#)]
37. Kim, G.; Shin, J.H. Luminescent Silicon-Rich Nitride Horizontal Air-Slot Microdisk Resonators for Biosensing. *IEEE Photonics Technol. Lett.* **2016**, *28*, 2331–2334. [[CrossRef](#)]
38. Park, H.G.; Kim, S.H.; Kwon, S.H.; Ju, Y.G.; Yang, J.K.; Baek, J.H.; Kim, S.B.; Lee, Y.H. Electrically Driven Single-Cell Photonic Crystal Laser. *Science* **2004**, *305*, 1444–1447. [[CrossRef](#)]
39. Fujita, M.; Ushigome, R.; Baba, T. Continuous Wave Lasing in GaInAsP Microdisk Injection Laser with Threshold Current of 40 μ A. *Electron. Lett.* **2000**, *36*, 790–791. [[CrossRef](#)]
40. Ren, Y.; Zhang, R.; Ti, C.; Liu, Y. Tapered Optical Fiber Loops and Helices for Integrated Photonic Device Characterization and Microfluidic Roller Coasters. *Optica* **2016**, *3*, 1205–1208. [[CrossRef](#)]
41. Srinivasan, K.; Borselli, M.; Johnson, T.J.; Barclay, P.E.; Painter, O.; Stintz, A.; Krishna, S. Optical Loss and Lasing Characteristics of High-Quality-Factor AlGaAs Microdisk Resonators with Embedded Quantum Dots. *Appl. Phys. Lett.* **2005**, *86*, 151106. [[CrossRef](#)]
42. Zheng, Y.; Fang, Z.; Liu, S.; Cheng, Y.; Chen, X. High-Q Exterior Whispering-Gallery Modes in a Double-Layer Crystalline Microdisk Resonator. *Phys. Rev. Lett.* **2019**, *122*, 253902. [[CrossRef](#)]

-
43. Choi, S.J.; Peng, Z.; Yang, Q.; Choi, S.J.; Dapkus, P.D. Tunable Microdisk Resonators Vertically Coupled to Bus Waveguides Using Epitaxial Regrowth and Wafer Bonding Techniques. *Appl. Phys. Lett.* **2004**, *84*, 651–653. [[CrossRef](#)]
 44. Li, C.; Zhou, L.; Zheng, S.; Poon, A.W. Silicon Polygonal Microdisk Resonators. *IEEE J. Sel. Top. Quantum Electron.* **2006**, *12*, 1438–1449. [[CrossRef](#)]
 45. Koseki, S.; Zhang, B.; De Greve, K.; Yamamoto, Y. Monolithic Integration of Quantum Dot Containing Microdisk Microcavities Coupled to Air-Suspended Waveguides. *Appl. Phys. Lett.* **2009**, *94*, 051110. [[CrossRef](#)]
 46. Zhukov, A.E.; Kryzhanovskaya, N.V.; Moiseev, E.I.; Maximov, M.V. Quantum-Dot Microlasers Based on Whispering Gallery Mode Resonators. *Light Sci. Appl.* **2021**, *10*, 80. [[CrossRef](#)] [[PubMed](#)]
 47. Moiseev, E.I.; Kryzhanovskaya, N.V.; Kudashova, Y.V.; Maximov, M.V.; Kulagina, M.M.; Troshkov, S.I.; Lipovskii, A.A.; Korpijärvi, V.M.; Karjalainen, H.; Niemi, T.; et al. Microdisk Lasers Based on GaInNAsSb/GaAsN Quantum Well Active Region. *J. Phys. Conf. Ser.* **2015**, *643*, 012040. [[CrossRef](#)]
 48. Wang, G.; Jiang, X.; Zhao, M.; Ma, Y.; Fan, H.; Yang, Q.; Tong, L.; Xiao, M. Microlaser Based on a Hybrid Structure of a Semiconductor Nanowire and a Silica Microdisk Cavity. *Opt. Express* **2012**, *20*, 29472–29478. [[CrossRef](#)]
 49. Koshelev, K.; Kruk, S.; Melik-Gaykazyan, E.; Choi, J.H.; Bogdanov, A.; Park, H.G.; Kivshar, Y. Subwavelength Dielectric Resonators for Nonlinear Nanophotonics. *Science* **2020**, *367*, 288–292. [[CrossRef](#)]